Study of Hybrid Air Vehicles Stability using Computational Fluid Dynamics

M. Carrión[a], M. Biava[b], G.N. Barakos[c], D. Stewart[d]
CFD Laboratory, School of Engineering, University of Glasgow, G12 8QQ Glasgow, UK

This paper uses Computational Fluid Dynamics to predict aerodynamic damping of airships or hybrid air vehicles. This class of aircraft is characterised by large lifting bodies combining buoyancy and circulatory lift. Damping is investigated via forced oscillations of the vehicle in pitch and yaw. The employed method is verified using data for lighter than air vehicles. The use of fins and stabilisers was found to be beneficial. The rear part of the body was dominated by separated flow that contained more frequencies than the forcing frequency imposed on the body. The final design is seen to be dynamically stable across a range of conditions for small pitch angles.

Nomenclature

$\dot{q}$	Rate of change of the pitching rate
$C_{M_y}^{\alpha}$	Longitudinal static stability derivative
$C_{M_z}^{\beta}$	Directional static stability derivative
$C_{M_y}^{\dot{\alpha}} + C_{M_y}^{q}$	Longitudinal aerodynamic damping coefficient
$C_{M_z}^{\dot{\beta}} + C_{M_z}^{r}$	Directional aerodynamic damping coefficient
C_D	Drag coefficient: $C_D = \frac{D}{\frac{1}{2}\rho_\infty U_\infty^2 Q^{2/3}}$
C_f	Friction coefficient: $C_f = \frac{\mu \frac{\partial u}{\partial n}}{\frac{1}{2}\rho_\infty U_\infty^2}$
C_L	Lift coefficient: $C_L = \frac{L}{\frac{1}{2}\rho_\infty U_\infty^2 Q^{2/3}}$
C_N	Normal force coefficient: $C_N = \frac{N}{\frac{1}{2}\rho_\infty U_\infty^2 Q^{2/3}}$
C_p	Pressure coefficient: $C_p = \frac{p-p_\infty}{\frac{1}{2}\rho_\infty U_\infty^2}$
C_S	Side force coefficient: $C_S = \frac{S}{\frac{1}{2}\rho_\infty U_\infty^2 Q^{2/3}}$
C_T	Tangential force coefficient: $C_T = \frac{T}{\frac{1}{2}\rho_\infty U_\infty^2 Q^{2/3}}$

[a] Research Associate, CFD Laboratory, School of Engineering. Email: Marina.Carrion@glasgow.ac.uk
[b] Research Associate, CFD Laboratory, School of Engineering. Email: Massimo.Biava@glasgow.ac.uk
[c] Professor, MAIAA, MRAeS, CFD Laboratory, School of Engineering. Email: George.Barakos@glasgow.ac.uk, corresponding author
[d] Hybrid Air Vehicles Ltd. Email: David.Stewart@HybridAirVehicles.net

C_{M_x}	Rolling moment coefficient: $C_{M_x} = \frac{M_x}{\frac{1}{2}\rho_\infty U_\infty^2 Q}$
C_{M_y}	Pitching moment coefficient: $C_{M_y} = \frac{M_y}{\frac{1}{2}\rho_\infty U_\infty^2 Q}$
C_{M_z}	Yawing moment coefficient: $C_{M_z} = \frac{M_z}{\frac{1}{2}\rho_\infty U_\infty^2 Q}$
F_i	Vector of inviscid fluxes
F_v	Vector of viscous fluxes
L	Vehicle length
L_{ref}	Reference length
n_c	Number of cycles
N_H	Number of harmonics
N_T	Number of time instances ($N_T = 2N_H + 1$)
Q	Hull volume)
q	Pitching rate
Re	Reynolds number
T	Period of oscillation)
t	Time
T^*	Non-dimensional period of oscillation
t_c	Characteristic time
U_∞	Free-stream velocity
V	Cell volume
x, y, z	Cartesian coordinates
BILU	Block Incomplete Lower-Upper
CFD	Computational Fluid Dynamics
CFL	Courant–Friedrichs–Lewy condition
H.B.	Harmonic Balance
HAV	Hybrid Air Vehicle

HMB Helicopter Multi-Block

LTA Lighter Than Air (Vehicle)

MUSCL Monotone Upwind Schemes for Scalar Conservation Laws

NS Navier-Stokes

RANS Reynolds Averaged Navier-Stokes

SPH Spheroid

SST Shear Stress Tensor

URANS Unsteady Reynolds Averaged Navier-Stokes

$\mathbf{R}$ Flux Residual

α Angle of attack

α_0 Mean angle of attack

α_1 Rate of change of the angle of attack

β Yaw angle

β_0 Mean yaw angle

β_1 Yaw oscillation amplitude

Δt Time-step

Δt^* Non-dimensional time-step

κ Reduced frequency ($\kappa = \pi/T$)

Ω Vorticity magnitude

ω Non-dimensional frequency of oscillation ($\omega = 2\kappa$)

$\overline{\omega}$ Frequency of oscillation

ρ Density)

θ Angle of pitch

I. Introduction

Airships, including lighter than air (LTA) and hybrid air vehicles (HAV), are large bodies combining buoyancy and circulatory lift. Due to the shape of the vehicle, the aerodynamic moments lead to nominally unstable configurations [1]. This is due to the fact that substantial parts of the aerodynamic lift are generated at the forward part of the hull. Wind tunnel experiments on the AKRON [2], YEZ-2A [3] and ZHIYUAN-1 [4, 5] airships are available in the literature. All of them presented static unstable behaviour, as the rigid models were employed and buoyancy was not accounted for.

Stability derivatives are important in dynamic and kinematic models of airships. These derivatives are traditionally obtained through flight test data [6], wind tunnel measurements [3] and engineering models [7, 8]. The first two approaches are costly and difficult to perform accurately. In addition, the flows around airships are highly vortical [9] and these large vortical structures need to be accounted for. This is possible with potential flow theory, but it requires extensive corrections and geometry simplifications. With this regard, Computational Fluid Dynamics (CFD) is a more accurate method, as complex geometries can be modelled and the vortical structures and interaction between components can be accounted for. Hence, if CFD is validated with wind tunnel data or flight test experiments, it can be a very efficient tool for stability analysis. Combined with methods like the harmonic balance [10] the CPU time for stability analyses is also reduced.

In the literature, Wang [11] computed the stability derivatives of the ZHIYUAN-1 airship from CFD solutions. Forced heaving motion and pitch oscillations (at reduced frequencies of 0.06 and 0.1) were studied and results on the bare hull and hull with fins were compared. The bare hull case was unstable, while the vehicle became stable when fins were included. Other works employed CFD for the calculation of stability derivatives for fixed wings [12, 13].

Given that HAVs have much more complex shapes than LTAs and that, to date, there is no study published on the stability of HAVs, it is the objective of this paper to perform longitudinal and directional stability studies for HAVs. In addition, CFD has been hardly used in the literature in the analysis of this type of aircraft [9] and this is also the case for stability studies using CFD instead of simpler aerodynamic models. Therefore, this paper also aims to assess the benefits and penalties of time-marching and harmonic balance methods to solve this type of problems. An idealised prolate spheroid (single-lobe body) is first used due to available experimental data, before attempting to investigate the flow and stability of a multi-lobe body (MLB) that approximates better the shape of a HAV. The effect of the aerodynamic surfaces in its dynamic and static stability is quantified.

II. Numerical Method

A. HMB3 flow solver

The Helicopter Multi-Block (HMB3) CFD solver [14, 15], developed at University of Glasgow, is used for the present work, and has so far been validated for a number of applications, including helicopters, wind turbines, turboprop and UCAV aircraft. HMB3 solves the Navier-Stokes equations in integral form using the

Arbitrary Lagrangian Eulerian (ALE) formulation for time-dependent domains with moving boundaries:

$$\frac{\mathrm{d}}{\mathrm{d}t}\int_{V(t)} \mathbf{W} dV + \int_{\partial V(t)} \left[F_i\left(\mathbf{W}\right) - F_v\left(\mathbf{W}\right)\right] \mathbf{n}\, dS = 0 \tag{1}$$

where $V(t)$ is the time dependent control volume, $\partial V(t)$ its boundary, $\mathbf{W}$ is the vector of conserved variables $[\rho, \rho u, \rho v, \rho w, \rho E]^T$, and F_i and F_v are the inviscid and viscous fluxes, including the effects of the mesh movement.

The Navier-Stokes equations are discretised using a cell-centred finite volume approach on a multi-block grid, leading to the following equations:

$$\frac{\partial}{\partial t}\left(\mathbf{W}_{i,j,k} V_{i,j,k}\right) = -\mathbf{R}_{i,j,k}\left(\mathbf{W}_{i,j,k}\right) \tag{2}$$

Here $\mathbf{W}_{i,j,k}$, $\mathbf{R}_{i,j,k}$ and $V_{i,j,k}$ represent the flow variables, the flow equation residuals and the volume of the cell with indices i, j and k, respectively. Osher's [16] upwind scheme is used for the discretisation of the convective terms and MUSCL [17] variable extrapolation is used to provide a formally 3rd order accurate scheme. To account for low-speed flows, the Low-Mach Roe scheme (LM-Roe) developed by Rieper [18] is employed [19]. The linearised system is solved using the generalised conjugate gradient method with a block incomplete lower-upper (BILU) pre-conditioner [20]. The HMB3 solver has a library of turbulence closures which includes several one- and two-equation turbulence models and versions of the k-ω model, including the scale-adaptive simulation (SAS) model [21], the Explicit Algebraic Stress k-ω model (EARSM) [22], and the γ-Re_{θ_t} transition model [23].

B. Harmonic balance method

HMB3 implements the harmonic balance method [10], that allows for a direct calculation of a periodic flow state. If the flow is assumed to be periodic with frequency ω, and approximated with N_H Fourier modes, the solution is represented by $N_T = 2N_H + 1$ discrete, equally spaced, time instances over the period $T = 2\pi/\omega$. Given the N_T instances, the time-domain solution for the cell (i, j, k) can be reconstructed using the following formula:

$$W \approx W_{T0} + \sum_{n=1}^{N_H} \Big(W_{Ta_n} \cos(\omega n t) + W_{Tb_n} \sin(\omega n t) \Big) \tag{3}$$

where W_{T0}, $W_{Ta,n}$ and $W_{Tb,n}$, $n = 1, \ldots, N_H$, are the Fourier coefficients of the flow variables $\mathbf{W} = [W_1 \ldots W_{N_T}]^T$, and the cell indices have been omitted to simplify the notation. If we set $\mathbf{W}_T = [W_{T0}\, W_{Ta,1}\, W_{Tb,1} \ldots W_{Ta,N_H}\, W_{Tb,N_H}]^T$, then Eq. (3) can be written in matrix form as

$$\mathbf{W} = \mathbf{E}\mathbf{W}_T \tag{4}$$

with the matrix $\mathbf{E}$ given by

$$\mathbf{E} = \begin{bmatrix} 1 & \cos(\omega t_1) & \sin(\omega t_1) & \ldots & \cos(N_H \omega t_1) & \sin(N_H \omega t_1) \\ 1 & \cos(\omega t_2) & \sin(\omega t_2) & \ldots & \cos(N_H \omega t_2) & \sin(N_H \omega t_2) \\ \vdots & \vdots & \vdots & \ddots & \vdots & \vdots \\ 1 & \cos(\omega t_{N_T}) & \sin(\omega t_{N_T}) & \ldots & \cos(N_H \omega t_{N_T}) & \sin(N_H \omega t_{N_T}) \end{bmatrix} \tag{5}$$

C. Computation of stability derivatives

To compute the stability derivatives associated to the vehicle pitching dynamics, a purely pitching motion is applied [24]. The motion is assumed to be sinusoidal, and the angle of pitch θ is equal to the angle of attack α:

$$\alpha = \theta = \alpha_0 + \alpha_1 \sin(\omega t) \tag{6}$$

where α_0 is the mean pitching angle, α_1 is the amplitude of the pitching motion and $\omega = 2\kappa$ is the non-dimensional frequency of oscillation, κ being the reduced frequency. The reduced frequency is related to the non-dimensional period T^* as $\kappa = \pi/T^*$. Note that the period is non-dimensionalised with the characteristic time $T^* = T/t_c$, defined by $t_c = L_{ref}/U_\infty$, with $L_{ref} = Q^{1/3}$ and Q the volume of the vehicle. From Eq. (6) results that the rate of change of the vehicle angle of attack $\dot{\alpha}$ and the pitching rate q are related by the following equations:

$$\dot{\alpha} = q = \omega \alpha_1 \cos(\omega t) \tag{7}$$

$$\ddot{\alpha} = \dot{q} = -\omega^2 \alpha_1 \sin(\omega t) \tag{8}$$

Using linear theory, the pitching harmonic response can be written as

$$\Delta C_{M_y} = C^{\alpha}_{M_y}(\alpha - \alpha_0) + C^{q}_{M_y} q + C^{\dot{\alpha}}_{M_y} \dot{\alpha} + C^{\dot{q}}_{M_y} \dot{q} \tag{9}$$

The CFD solution for the forced oscillation can be expressed as a truncated Fourier series. Ignoring the high order harmonics, we have:

$$\Delta C_{M_y} = A_1 \sin(\omega t) + B_1 \cos(\omega t) \tag{10}$$

Comparing Eqs. (9) and (10), and using Eqs. (6)-(8), it follows that

$$A_1 = \left(C^{\alpha}_{M_y} - \omega^2 C^{\dot{q}}_{M_y} \right) \alpha_1, \tag{11}$$

$$B_1 = \left(C^{\dot{\alpha}}_{M_y} + C^{q}_{M_y} \right) \alpha_1 \omega \tag{12}$$

The Fourier coefficients A_1 and B_1 can be computed using the usual formulas:

$$A_1 = \frac{2}{\alpha_1 n_c T} \int_0^{n_c T} C_{M_y}(t) \sin(\omega t) dt, \tag{13}$$

$$B_1 = \frac{2}{\alpha_1 \omega n_c T} \int_0^{n_c T} C_{M_y}(t) \cos(\omega t) dt \tag{14}$$

where the integrals are extended over n_c cycles of the periodic solution. The out-of-phase component B_1 represents an aerodynamic damping term, with a contribution from the rate of change of the angle of attack ($C^{\dot{\alpha}}_{M_y}$), and a contribution from the pitching rate ($C^{q}_{M_y}$). The in-phase component A_1 is composed by a static derivative ($C^{\alpha}_{M_y}$) and by a term associated to the second derivative of the pitch angle ($C^{\dot{q}}_{M_y}$).

It is possible to split the two contributions to the in-phase component by considering two different pitching conditions (a) and (b), where the mean angle α_0 and the amplitude of the oscillation α_1 are kept constant, and the reduced frequency is changed. In fact, the following two relations hold:

$$A_{1_a} = \left(C^{\alpha}_{M_y} - \omega_a^2 C^{\dot{q}}_{M_y}\right)\alpha_1, \tag{15}$$

$$A_{1_b} = \left(C^{\alpha}_{M_y} - \omega_b^2 C^{\dot{q}}_{M_y}\right)\alpha_1 \tag{16}$$

which can be inverted, to give

$$C^{\dot{q}}_{M_y} = \frac{A_{1_a} - A_{1_b}}{\alpha_1(\omega_b^2 - \omega_a^2)}, \tag{17}$$

$$C^{\alpha}_{M_y} = \frac{A_{1_a} + C^{\dot{q}}_{M_y}\omega_a^2\alpha_1}{\alpha_1} \tag{18}$$

The described procedure can be used to compute other stability derivatives, provided that the relevant dynamics is excited by the imposed motion, and that the correct linearisation is of the forces and moments is used.

III. Mesh generation

Multi-block structured topologies were employed, to allow for an accurate representation of the spheroid and airship surfaces. The blocks were also used to allow for an easy sharing of the computational load between processors for parallel computing. Figure 1 shows the surface mesh for the 6:1 prolate spheroid, the multi-lobe hull and the multi-lobe hull with tail aerodynamic surfaces.

For the spheroid grid, an "O"-type topology was employed, with a total of 160 blocks for good load balancing between processors. The inflow, outflow and far-field boundaries extended 10L from the spheroid surface (see Fig. 2a). Since the spheroid was employed to assess the forced oscillations method, a coarse grid with 1.2 million cells was employed, to reduce the cost of the unsteady computations.

The grids for the multi-lobe body, with and without tail aerodynamic surfaces, are more more complex and need a higher number of cells to accurately represent the aerodynamic flow field. The bare hull grid has 1,069 blocks and 9.2 million of cells. The grid including the tail surfaces has 1,203 blocks and 10.8 million of cells. A set of sliding planes [25] were employed, to allow for localised grid refinement near the body and to have a cartesian grid in the rest of the domain. These planes are shown in Fig. 2b. Note that a grid refinement study was performed for this multi-lobe body in Ref. [9]. The length L of the multi-lobe body is representative of a large-scale vehicle and is approximately $120\,\mathrm{m}$, the total width is $60\,\mathrm{m}$ and the three spheroids occupy a volume of $100,000\,\mathrm{m}^3$.

Under the assumption of a symmetric flow, only half of the body was meshed for the pitch oscillations cases. On the other hand, the full body was needed for the yaw cases. At the inflow, outflow and far-field boundaries, free-stream conditions were assumed. A first cell-layer size of $3 \cdot 10^{-6}$ L was employed, to ensure that $y^+ \approx 1$. Table 1 provides a summary of properties of the employed meshes.

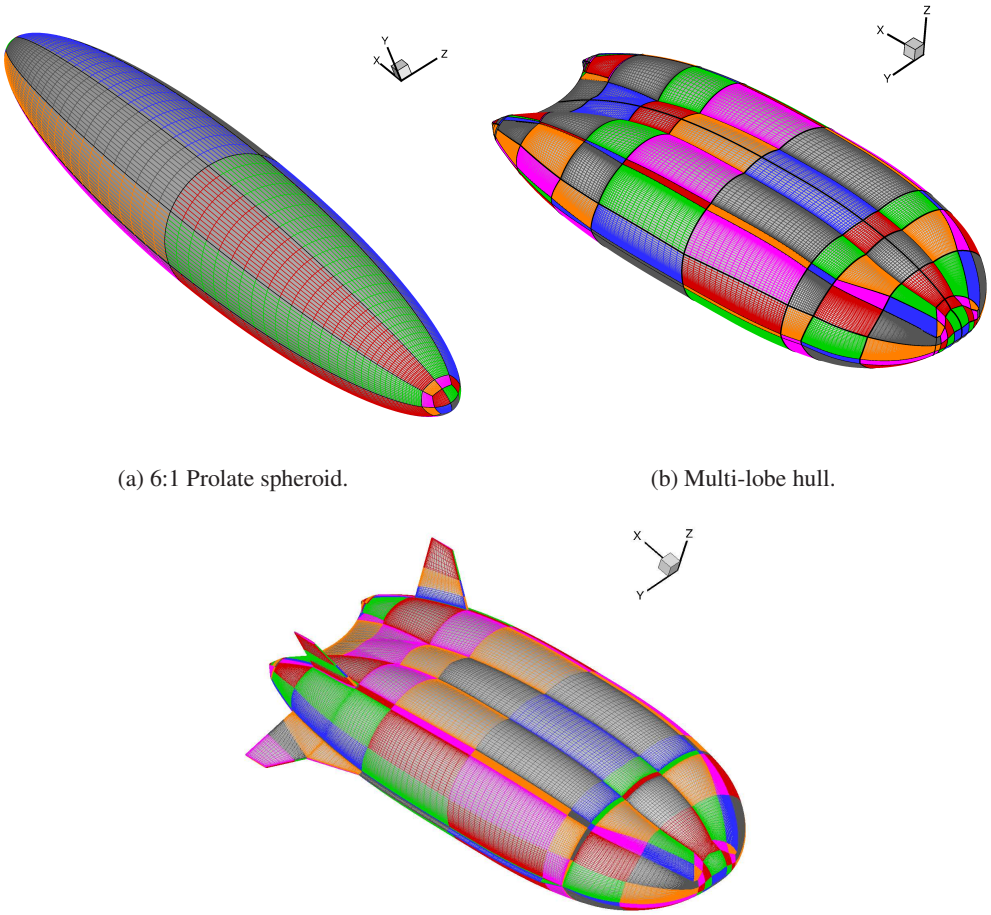

(a) 6:1 Prolate spheroid.

(b) Multi-lobe hull.

(c) Multi-lobe hull with tail aerodynamic surfaces.

Fig. 1: Multi-block surface meshes.

Table 1: Summary of mesh properties. Mesh size in million of cells.

Case	Size (Blocks)	Cross sect.-(span)-wise cells	CPUs
Spheroid	1.2M (160)	112 (116)	16
HULL	9.2M (1,069)	236 (314)	48
MLB	10.8M (1,203)	236 (314)	48

IV. Numerical results

For the spheroid cases (SPH), a Reynolds number of 4.3 million (based on the spheroid length), and a Mach number of 0.15 were employed. For the multi-lobe body cases, bare hull (HULL) and hull with aerodynamic surfaces (MLB), a Reynolds number of 3 million (based on the hull length) and a Mach number of 0.12 were selected. The k-ω SST turbulence model [26] was employed for all the simulations.

Table 2 summarises the cases for the longitudinal stability study. Two scenarios were considered: oscil-

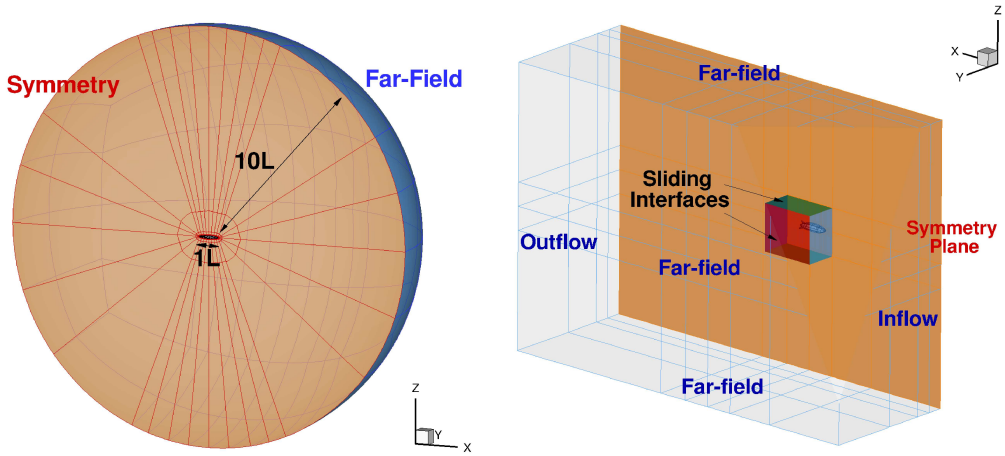

(a) 6:1 Prolate spheroid.

(b) Multi-lobe hull.

Fig. 2: Computational domain and boundary conditions.

Table 2: Properties of forced pitching cases.

ID	α_0 [°]	α_1 [°]	κ [-]	T^* [-]	ω [-]	Δt^* [-]
SPH1	0	5	0.45	7.03	0.89	0.035
SPH2	15	5	0.05	62.8	0.1	0.314
HULL1	0	2	0.05	62.8	0.1	0.063
HULL2	15	5	0.05	62.8	0.1	0.063
HULL3	0	2	0.05	62.8	0.1	0.314
HULL4	15	5	0.05	62.8	0.1	0.314
HULL5	0	2	0.1	31.4	0.2	0.157
HULL6	15	5	0.1	31.4	0.2	0.157
HULL7	0	2	0.2	15.7	0.4	0.079
HULL8	15	5	0.2	15.7	0.4	0.079
HULL9	0	2	0.01	314	0.02	1.570
MLB1	0	2	0.05	62.8	0.1	0.314
MLB2	15	2	0.05	62.8	0.1	0.314
MLB3	15	5	0.05	62.8	0.1	0.314
MLB4	0	2	0.1	31.4	0.2	0.157
MLB5	15	2	0.1	31.4	0.2	0.157
MLB6	15	5	0.1	31.4	0.2	0.157

lations about zero angle of attack, and oscillations about a large mean angle of attack ($15°$). The amplitude of the oscillations was $\pm 2°$ for the former scenario, while amplitudes of $\pm 2°$ and $\pm 5°$ were considered for the latter. For the zero mean angle of attack, no flow separation was present and the linear response approximation is expected to be very accurate. For the higher mean angle of attack, separation at the rear of the vehicle was observed, and the linear approximation can be less representative of the actual vehicle dynamics.

Table 3: Properties of forced yawing cases.

ID	β_0 [°]	β_1 [°]	κ [-]	T^* [-]	ω [-]	Δt^* [-]
MLBD1	0	2	0.05	62.8	0.1	0.314
MLBD2	0	2	0.1	31.4	0.2	0.157

Reduced frequencies κ of 0.01, 0.05, 0.1 and 0.2 were studied.

The configuration with tail aerodynamic surfaces (MLB) was employed for the study of the directional stability. Table 3 provides a summary of the computations. Low amplitude oscillations ($\pm 2°$) around zero mean yaw angle were considered. The same reduced frequencies as for the pitching cases were used.

A. Effect of the time step size

The effect of the CFD time steps was first investigated. In the first set of computations (cases HULL1 and HULL2), 1000 steps were performed per cycle ($\Delta t = T/1000$). In the second set of computations (cases HULL3 and HULL4), 200 steps were performed per cycle ($\Delta t = T/200$). Figure 3 shows the hysteresis loops of the normal force coefficient C_N, obtained with both time step sizes. For small oscillations (Fig. 3a), there are very small differences in the hysteresis loops. For the more demanding cases HULL2 and HULL4, shown in Fig. 3b, the mean value is the same for both cases; however, the peak-to-peak values are larger for the smaller time step. These differences are due to a different separation pattern at the rear of the vehicle, as can be seen in the contours of vorticity magnitude of Fig. 4. This affects the pressure distribution in that region, as shown later in Fig. 8. It was found that three cycles were enough to achieve loads convergence. This is confirmed by the hysteresis loops of Fig. 3b, the solutions on the second and third cycles are practically identical.

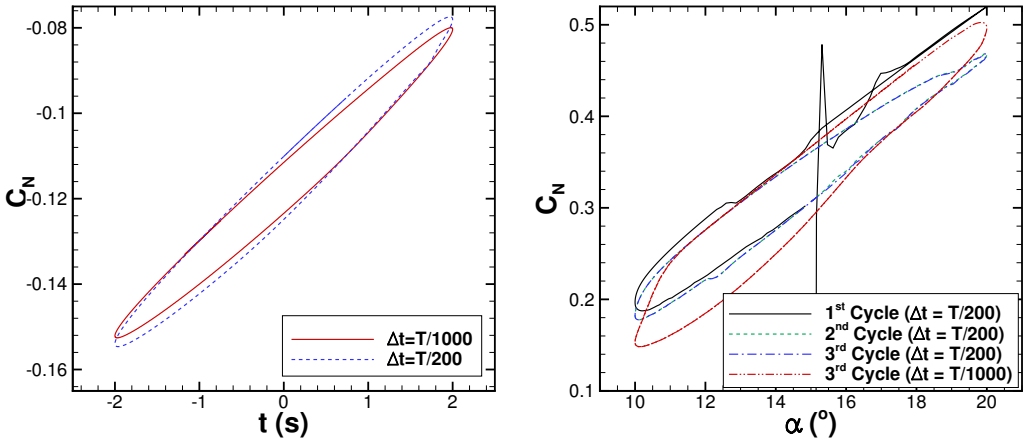

(a) $\alpha_0 = 0°$, $\alpha_1 = 2°$, $\kappa = 0.05$ (cases HULL1 and HULL3)

(b) $\alpha_0 = 15°$, $\alpha_1 = 5°$, $\kappa = 0.05$ (cases HULL2 and HULL4)

Fig. 3: Effect of the time step size, showing convergence behaviour.

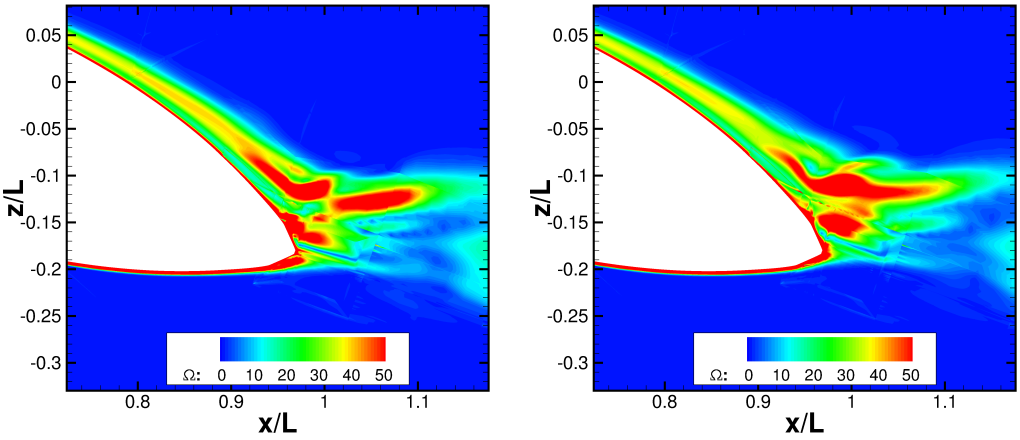

(a) $\Delta t = T/1000$ (case HULL2).

(b) $\Delta t = T/200$ (case HULL4).

Fig. 4: Effect of the time step size in the separation pattern at the back of the hull.

B. Evaluation of the harmonic balance method

The Harmonic Balance method enables the convergence of periodic flows faster than time-marching methods. However, this method has some restrictions related to the number of modes N_H that can be employed, as the memory required increases with a factor $N_T = 2N_H + 1$. To properly capture very complex flows, the number of required modes can be large, and the harmonic balance method becomes less competitive than time marching.

This section aims to evaluate the feasibility of using the harmonic balance for MLB flows. The first part of this study concerned the flow around a 6:1 prolate spheroid and the solutions were compared with the data published by Wang [11]. In the second part, the flow around the MLB is analysed.

For both the prolate spheroid and the MLB, the origin of the pitch axis was assumed to be the centre of volume. This point was also used to evaluate the pitching and yawing moments.

1. 6:1 prolate spheroid

The HMB3 CFD solver is validated with the data on a 6:1 pitching spheroid published by Wang [11]. For this case, a two million-cell grid was employed. The spheroid was forced to pitch around a mean pitch angle of $\alpha_0 = 0°$, with amplitude of $\alpha_1 = 5°$ and at a reduced frequency of $\kappa = 0.447$ (case SPH1). Figure 5 shows the pitching moment M_y over one cycle. As can be observed, both CFD solutions (time-accurate and harmonic balance with 3 modes) agree perfectly with the signal provided by Wang [11].

A second test was performed for the spheroid (case SPH2). The pitching moment coefficient and the surface pressure at one instance, shown in Figs. 6a and 6b, respectively, demonstrate that the time-accurate and harmonic balance solutions are almost identical, even for very high pitch conditions. To complete 3 cycles, the time-marching computations took 48 hours using 16 processors. Using the harmonic balance

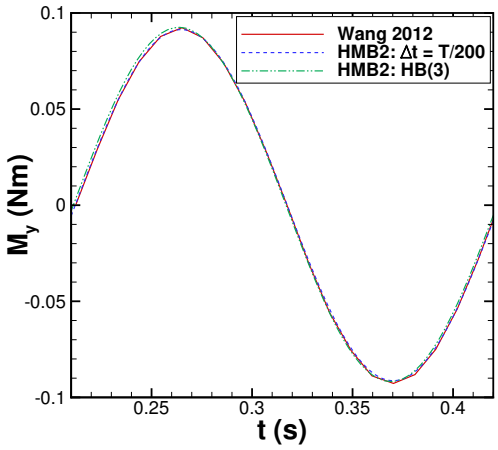

Fig. 5: Validation of time-accurate and harmonic balance methods with results by Wang [11] (case SPH1).

method, half of the time was required. These results show that for idealised flows, such as those around spheroids, the harmonic balance method allows for great savings in computational time.

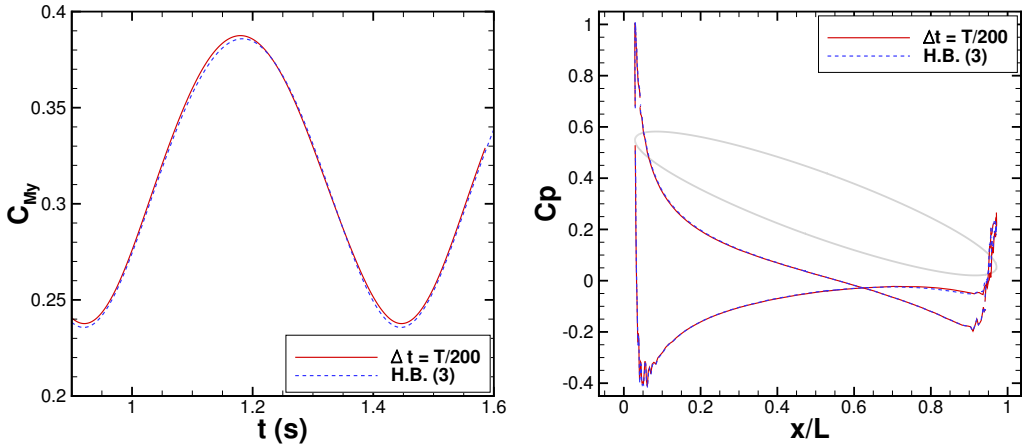

(a) Pitching moment signal.

(b) Surface pressure coefficient.

Fig. 6: Comparison between time-accurate and harmonic balance methods of HMB3 (case SPH2).

2. *Multi-lobe body*

The harmonic balance method was also evaluated for the MLB and three scenarios were considered:

- small pitching oscillations ($\alpha_1 = 2°$) around $\alpha_0 = 0°$ for the bare hull, $\kappa = 0.05$, $\Delta t = T/200, T/1000$ (cases HULL1 and HULL3);
- large pitching oscillations ($\alpha_1 = 5°$) around $\alpha_0 = 15°$ for the bare hull, $\kappa = 0.05$, $\Delta t = T/200, T/1000$ (cases HULL2 and HULL4);

- small pitching oscillations ($\alpha_1 = 2°$) around $\alpha_0 = 15°$ for the MLB with tail aerodynamic surfaces, $\kappa = 0.05$, $\Delta t = T/200$ (case MLB2).

These are much more complex flows with respect to the spheroid case, with the presence of large separation areas, especially for the higher mean angle of attack scenarios. For all cases, only 2 harmonics were employed, to enable for fast computations with limited memory requirements.

Harmonic balance and time-marching tangential force signals are compared in Fig. 7a for the first scenario. As can be observed, the signals obtained with the small time step and the harmonic balance are in very good agreement. It should be mentioned that for the normal force and the pitching coefficients, the discrepancy between harmonic balance and time-marching solutions is even smaller, and they are not shown here. The harmonic balance method relies on the hypothesis that the flow to be computed is periodic. This is possible for this case, as small oscillations were considered and the flow is attached. In addition, the use of this method is highly beneficial, as the converged solution was obtained in half the time needed for the time-marching computations.

The second scenario is presented in Fig. 7b. The harmonic balance and time-marching solutions have very similar mean values, but there are differences in the amplitude of the oscillations, especially around $t = 0.9$s, that corresponds to the highest pitch ($\alpha = 20°$). Differences in the separation pattern affect the pressure distribution at the rear of the vehicle, as shown in Fig. 8. These differences maybe due to the fact that only 2 modes were employed for the harmonic balance solution. To capture such a complex behaviour, more modes are required. However, this would lead to longer computations and higher memory requirements.

The comparison relative to the third scenario is shown in Fig. 7c. The mean angle of attack is high ($\alpha_0 = 15°$) and separation at the back of the hull takes place. However, the small amplitude of the oscillations ($\alpha_1 = 2°$) leads to a solution with smaller frequency content, and the harmonic balance method with 2 modes is able to reproduce the time-marching solution with high accuracy. The computational time for the harmonic balance is less than half of the time-marching method.

These results demonstrate that the harmonic balance can be applied to hybrid air vehicles, and great benefits in terms of savings in computational time can be obtained, as long as small oscillations are considered. When complex flows are studied, such as those with large separation areas, large number of harmonics are required to fully capture the flow features, and the time-marching approach can be more efficient.

C. Longitudinal stability analysis

This section provides a study of the MLB's longitudinal stability. The effect of the aerodynamic surfaces is first analysed, and the sensitivity to the reduced frequency is then demonstrated. Finally, results about stability derivatives are presented.

1. Effect of the aerodynamic surfaces

Figures 9 and 10 present hysteresis loops of normal, tangential forces, and pitching moment around the centre of volume for the bare hull and the hull with aerodynamic surfaces. The loads obtained from

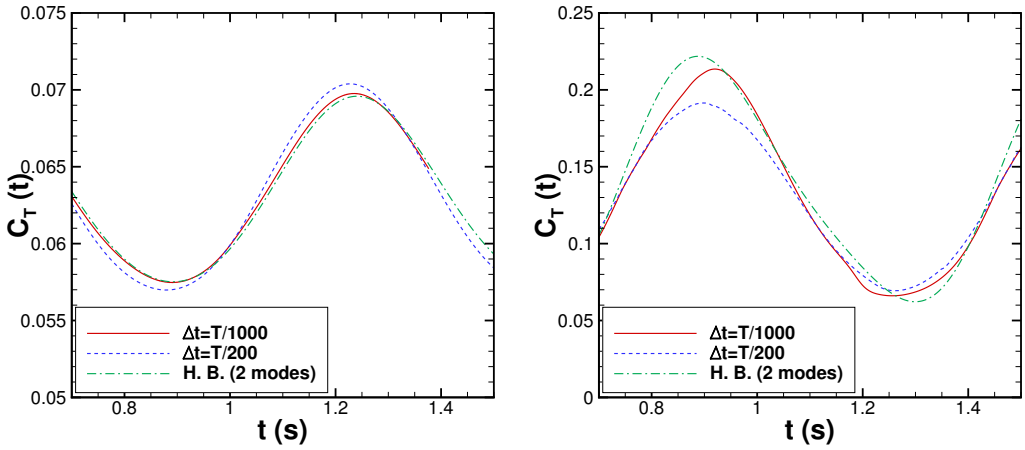

(a) $\alpha_0 = 0^\circ$, $\alpha_1 = 2^\circ$, $\kappa = 0.05$ (cases HULL1 and HULL3).

(b) $\alpha_0 = 15^\circ$, $\alpha_1 = 5^\circ$, $\kappa = 0.05$ (cases HULL2 and HULL4).

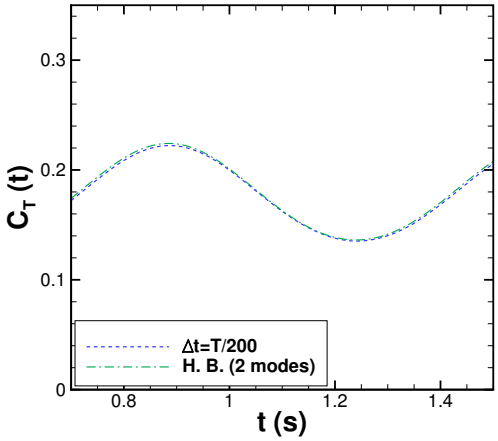

(c) $\alpha_0 = 15^\circ$, $\alpha_1 = 2^\circ$, $\kappa = 0.05$ (case MLB2).

Fig. 7: Effect of the time step size and harmonic balance on the tangential force C_T.

steady computations are also included as symbols. Note that the raw data is restricted and the loads were non-dimensionalised with the bare hull steady values at the mean pitch angle α_0.

For the case of small oscillations (Fig. 9), lift and drag increased, once the aerodynamic surfaces were included. The pitching moment was reduced in slope, which is indicative of a more stable vehicle. For this pitching case, the hysteresis was almost unaffected by the inclusion of the aerodynamic surfaces. Compared to steady computations, the tangential force was the mostly affected, with differences up to 10%.

Large amplitude oscillations at high pitch angle present a very different behaviour from the previous case, as shown in Fig. 10. The unsteady pitching motion affects more the bare hull than the MLB, as the steady and unsteady loads are closer to each other for the latter. In addition, once the aerodynamic components are included, there is a load oscillation that begins at $\alpha = 16^\circ$ and remains present until the peak pitch angle $\alpha_{\max} = 20^\circ$ is reached. This behaviour is not observed on the bare hull, which indicates that the fins stalled. At these high pitch angles there is no hysteresis effect. Since the fins are stalled, the vehicle

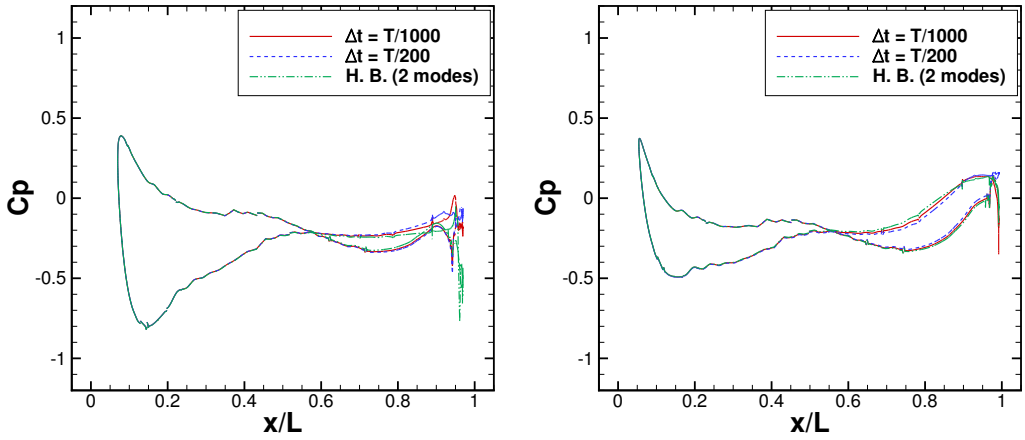

(a) Upwards.

(b) Downwards.

Fig. 8: Effect of the time step size and harmonic balance in the surface C_p on the side lobe (cases HULL2 and HULL4).

generates similar forces regardless of the pitching motion direction, upwards or downwards. Nevertheless, the aerodynamic surfaces have a stabilising effect, as the overall magnitude of the pitching moment and its slope are reduced.

2. *Effect of the reduced frequency*

The effect of the reduced frequency κ on the non-dimensional pitching moment is studied here. The hysteresis loops of the bare hull and the hull with aerodynamic surfaces at zero mean pitch angle are presented in Fig. 11. When the vehicle pitches fast (high reduced frequency), there is an increase in the hysteresis effect. When the pitching motion is slow (low reduced frequency), the hysteresis effect is reduced. Note, however, that the maximum and minimum values of C_{M_y} are not affected by the reduced frequency.

The effect at the higher mean pitch angle and oscillation amplitude ($\alpha_0 = 15°$, $\alpha_1 = 5°$) is shown in Fig. 12. Compared to the previous cases, the differences in pitching moment when the reduced frequency is changed are more significant, as shown in Fig. 12a. Also, for the case of the complete MLB configuration (Fig. 12b), pitching moment oscillations are observed around the maximum pitch angle $\alpha_{\max} = 20°$, whose amplitude becomes larger as the reduced frequency is increased.

3. *Aerodynamic derivatives*

The aerodynamic derivatives were obtained using the method presented in Sec. II C. The method was validated by reproducing the results obtained by Wang [11] for the Zhiyuan-1 airship. Table 4 shows the values presented in Ref. [11] and those computed with the current implementation of the method. Differences of less than 1.5% were obtained.

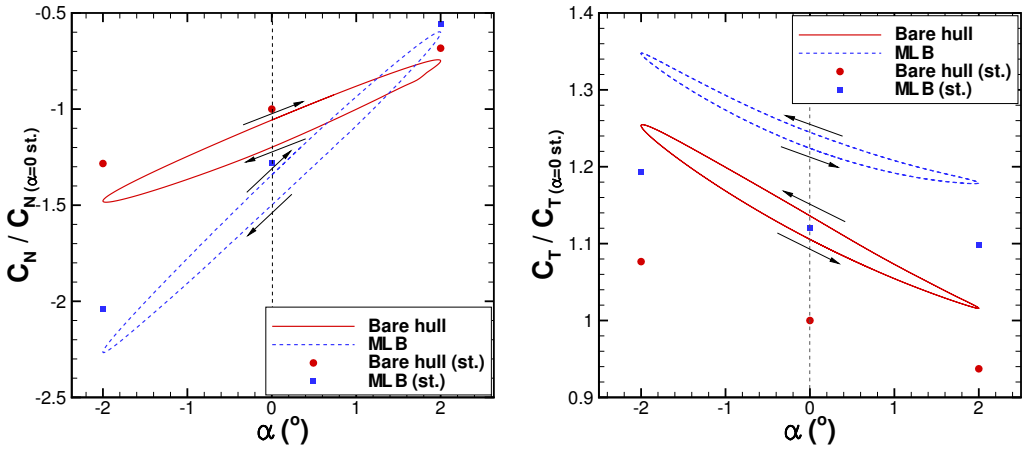

(a) Normal force.

(b) Tangential force.

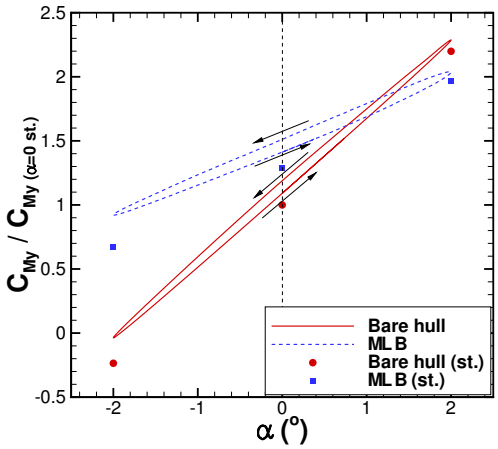

(c) Pitching moment.

Fig. 9: Hysteresis loops for cases HULL3 and MLB1 ($\alpha_0 = 0°$, $\alpha_1 = 2°$, $\kappa = 0.05$). Steady solutions (st.) included.

Coefficient	Hull	Hull and fins
$C^{\dot{\alpha}}_{F_z} + C^{q}_{F_z}$	-2.91265 (-2.8755)	-4.56493 (-4.4520)
$C^{\dot{\alpha}}_{M_y} + C^{q}_{M_y}$	0.12428 (0.2426)	-1.52128 (-1.5291)

Table 4: Pitching aerodynamic derivatives for the Zhiyuan-1 airship [11].

Table 5 provides a summary of the pitching moment damping and static coefficients. To respect the confidentiality of the data, the coefficients were non-dimensionalised using the absolute value of the bare hull coefficient at low pitching amplitude and reduced frequency $\kappa = 0.01$. As can be observed, the cases at low pitch are damped for both the bare hull and the hull including aerodynamic surfaces, as the damping coefficients are negative ($C^{\dot{\alpha}}_{M_y} + C^{q}_{M_y} < 0$). Conversely, the damping becomes positive when high pitch cases are considered ($C^{\dot{\alpha}}_{M_y} + C^{q}_{M_y} > 0$). The inclusion of the tail aerodynamic surfaces is not enough to

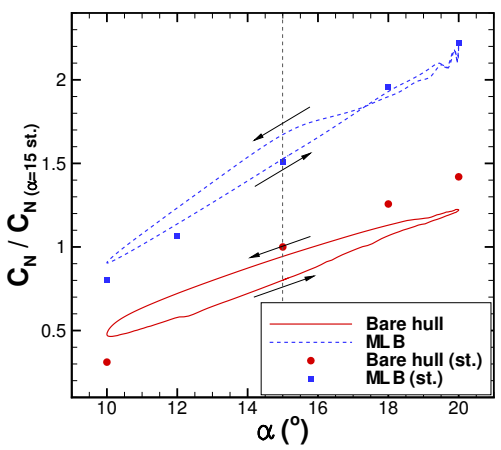

(a) Normal force.

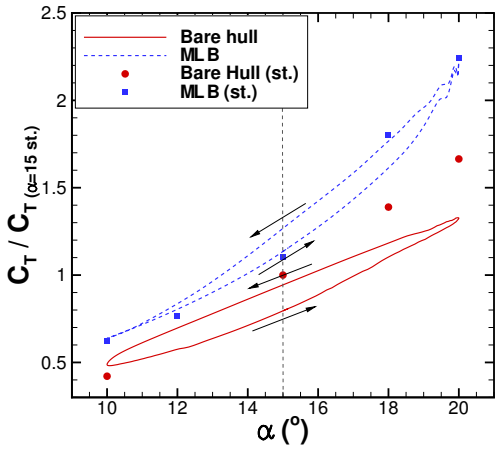

(b) Tangential force.

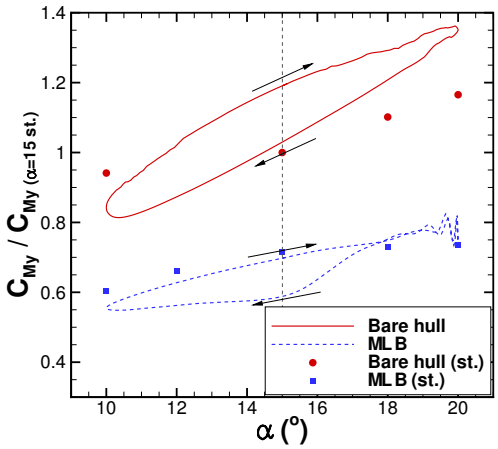

(c) Pitching moment.

Fig. 10: Hysteresis loops for cases HULL4 and MLB3 ($\alpha_0 = 15°$, $\alpha_1 = 5°$, $\kappa = 0.05$). Results from steady solutions (st.) included.

render the damping coefficient negative, but reduces its magnitude.

The static derivative $C^{\alpha}_{M_y}$ was also non-dimensionalised with the bare hull solution. Results show that this derivative has positive sign, regardless of the configuration, pitch angle and oscillation amplitude. Nevertheless, an improvement was obtained by including the tail aerodynamic surfaces, as $C^{\alpha}_{M_y}$ dropped by about 50% both at small and high pitch angles. These results are in good agreement with earlier works for the same vehicle [9]. It should be mentioned that in the present study the front and rear thrusters, that may affect the stability of the vehicle, were not accounted for in the simulations.

D. Directional Stability Analysis

This section provides a study of the MLB's directional stability. Figures 13 and 14 show the hysteresis loops of the force and moment coefficients, respectively, for the cases MLBD1 and MLBD2, which differ only in the reduced frequency of the yaw oscillations (κ =0.05 and 0.1). The loads were non-dimensionalised

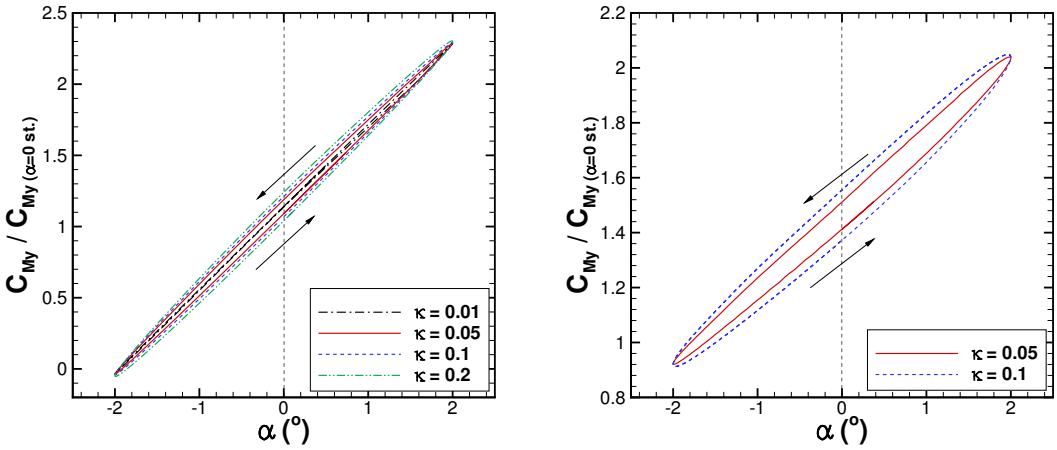

(a) Bare hull (cases HULL3, HULL5, HULL7 and HULL9).

(b) MLB (cases MLB1 and MLB4).

Fig. 11: Effect of the reduced frequency on the pitching moment ($\alpha_0 = 0°$, $\alpha_1 = 2°$, $\kappa = 0.01,\ 0.05,\ 0.1,\ 0.2$).

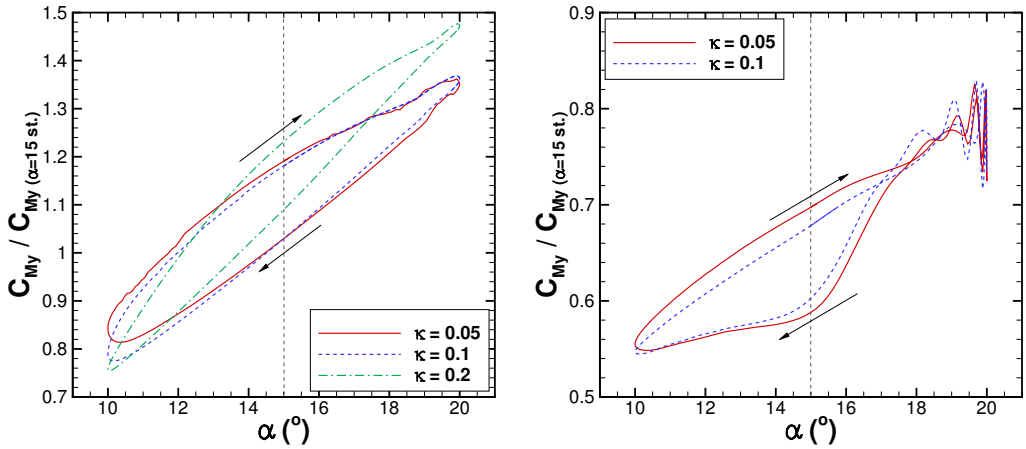

(a) Bare hull (cases HULL4, HULL6 and HULL8).

(b) MLB (cases MLB3 and MLB6).

Fig. 12: Effect of the reduced frequency on the pitching moment ($\alpha_0 = 15°$, $\alpha_1 = 5°$, $\kappa = 0.05,\ 0.1,\ 0.2$).

with the corresponding values in steady condition at zero pitch and yaw.

A non-symmetric behaviour is observed in the hysteresis loops, for both the forces and moments coefficients. This is due to flow separation at the fins and at the back of the vehicle, that is delayed with respect to the yawing movement. A faster yawing oscillation leads to an increase in the hysteresis of the side force and yawing moment, and to a more oscillatory pattern for the other quantities.

Table 6 provides the directional stability derivatives for the two considered cases. The coefficients were non-dimensionalised using the absolute value at reduced frequency of 0.05. As can be observed, both cases are dynamically stable ($C^{\dot{\beta}}_{M_z} + C^{r}_{M_z} < 0$), while the static derivatives are positive ($C^{\beta}_{M_z} > 0$).

Conditions			$\left(C^{\dot{\alpha}}_{M_y} + C^{q}_{M_y}\right)\omega\alpha_1$		$C^{\alpha}_{M_y}$	
α_0	α_1	κ	Bare Hull	MLB	Bare Hull	MLB
0°	2°	0.01	-1.0	-	1.00	0.48
		0.05	-15.0	-17.1		
		0.1	-21.6	-29.7		
		0.2	-31.7	-		
15°	2°	0.05	125.0	19.7	-	0.23
		0.1	120.0	8.2		
15°	5°	0.05	141.2	58.9	0.58	0.28
		0.1	131.7	31.1		
		0.2	100.9	-		

Table 5: Aerodynamic derivatives for the pitching cases.

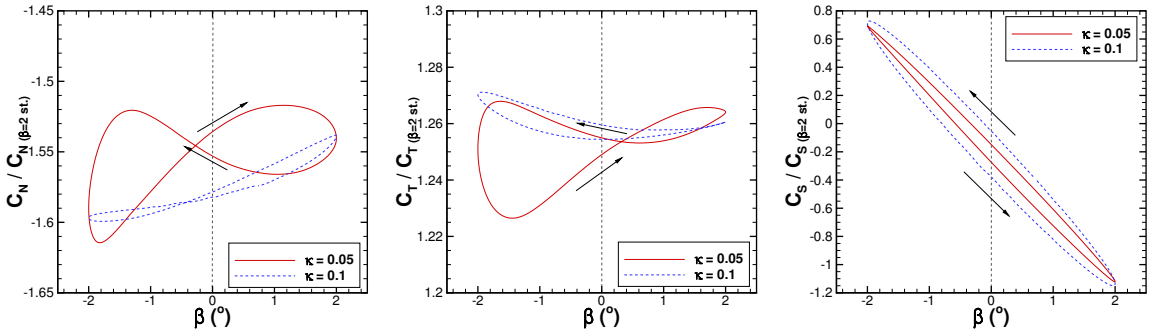

(a) Normal force. (b) Tangential force. (c) Side force.

Fig. 13: Hysteresis of the force coefficients for forced yaw oscillations (cases MLBD1 and case MLBD2, $\beta_0 = 0°$, $\beta_1 = 2°$, $\kappa = 0.05,\ 0.1$).

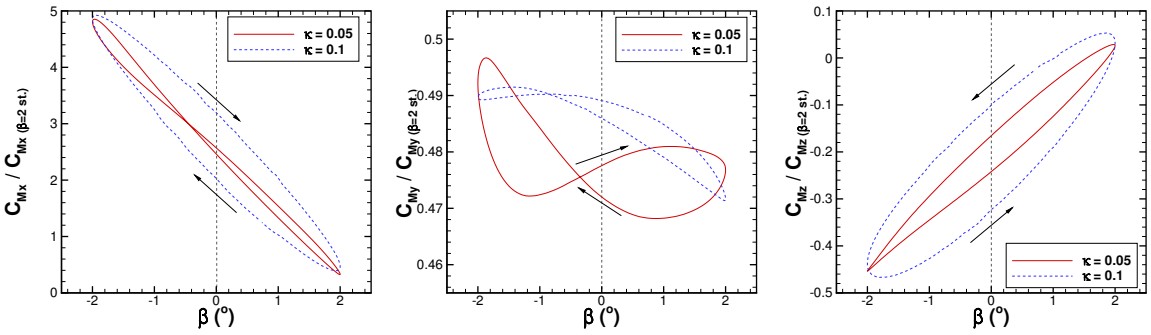

(a) Rolling moment. (b) Pitching moment. (c) Yawing moment.

Fig. 14: Hysteresis of the moment coefficients for forced yaw oscillations (cases MLBD1 and case MLBD2, $\beta_0 = 0°$, $\beta_1 = 2°$, $\kappa = 0.05,\ 0.1$).

β_0	β_1	κ	$\left(C^{\dot{\beta}}_{M_z} + C^{r}_{M_z}\right)$	$\omega\beta_1$	$C^{\beta}_{M_z}$
0°	2°	0.05	-1.0		0.1480
		0.1	-1.4		

Table 6: Stability derivatives for the yawing cases.

E. Flow Visualisation

Figure 15 presents flow visualisation at $85\%\ L$ over one pitch oscillation. Flow separation on the upper and lower fins indicate that these were in stall condition when large pitch amplitudes were considered, leading to the highly oscillatory force signals observed in the hysteresis loops of Fig. 10. Figure 16 shows the flow at the mid-height plane ($z = 0$) near the back of the vehicle, over one yaw oscillation. A non-symmetric separation pattern is observed, that leads to the non-symmetric hysteresis loops of Figs. 13 and 14.

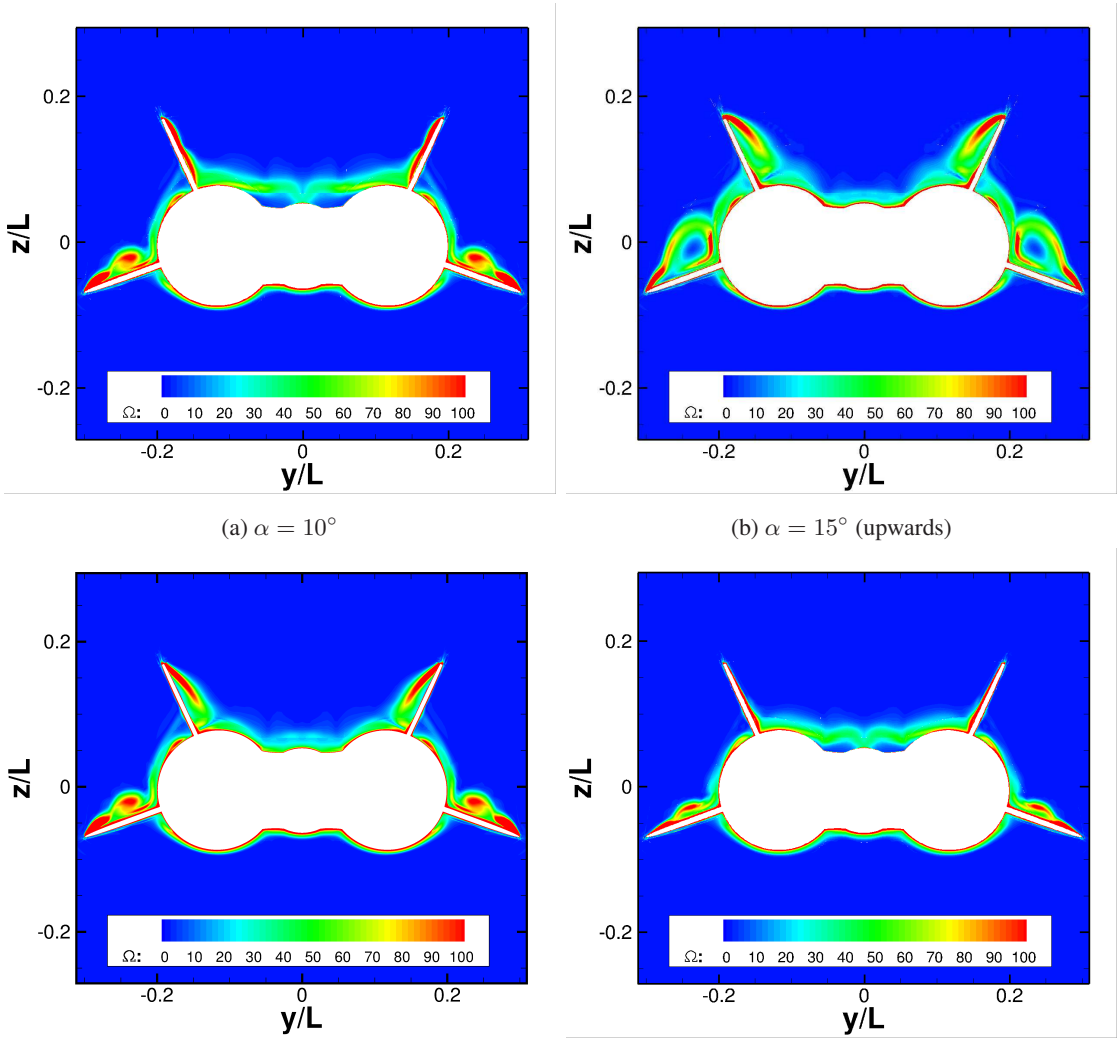

(a) $\alpha = 10^\circ$

(b) $\alpha = 15^\circ$ (upwards)

(c) $\alpha = 20^\circ$

(d) $\alpha = 15^\circ$ (downwards)

Fig. 15: Flow visualisation over one pitch oscillation (case MLB3, $\alpha_0 = 15^\circ$, $\alpha_1 = 5^\circ$, $\kappa = 0.05$).

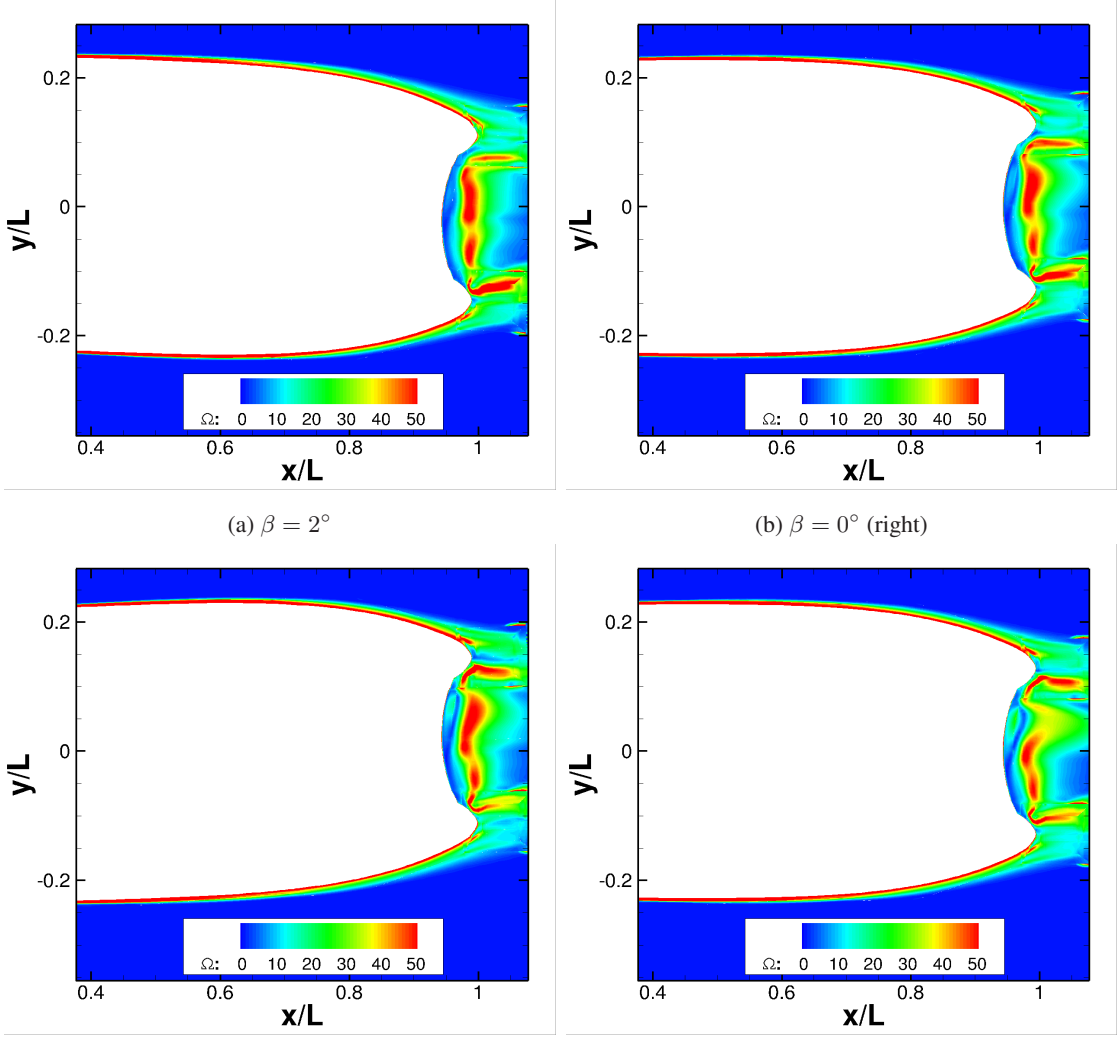

(a) $\beta = 2°$

(b) $\beta = 0°$ (right)

(c) $\beta = 2°$

(d) $\beta = 0°$ (left)

Fig. 16: Flow visualisation over one yaw oscillation (case MLBD1, $\beta_0 = 0°$, $\beta_1 = 2°$, $\kappa = 0.05$).

V. Conclusions

This paper investigated the aerodynamic stability derivatives of hybrid air vehicles using CFD. The feasibility of the use of the harmonic balance method for airship flows was also evaluated. For simple flows around spheroids, the time-marching and the harmonic balance solutions were practically identical, the latter allowing for great savings in computational time. For hybrid air vehicles, benefits in the use of the harmonic balance method were also obtained, as long as low amplitude oscillations were considered. When more complex flows are studied, such as those with large separation areas due to large amplitude oscillations, a large number of harmonics is required to fully capture the flow features and the cost is comparable or higher than the time-marching method.

Study of the longitudinal stability of the MLB showed that the aerodynamic surfaces have a stabilising effect. They contributed to reducing the magnitude of the damping derivatives for unstable cases. At low pitch angles, the reduction was 15% and 36%, for reduced frequencies of 0.05 and 0.1, respectively. At

high pitch angle, the reduction was 60% and 75%, respectively, for the same reduced frequencies. It was also noted that an increase in the frequency of oscillation led to an increase in the hysteresis effect of the aerodynamic loads and moments. Static pitching derivatives for the multi-lobe body showed positive values for all the considered conditions. However, the aerodynamic surfaces contributed to reduce magnitude of the unstable derivative.

The work also considered the directional stability of the vehicle. The separated flow at the back of the body was found to contain more frequencies than the forcing frequency, leading to non-symmetric hysteresis loops. In addition, the tested multi-lobe shape was found to be dynamically stable for the studied cases.

Acknowledgements

Results were obtained using the Jupiter cluster of CFD Lab of University of Glasgow and the EPSRC funded ARCHIE-WeST High Performance Computer (`www.archie-west.ac.uk`), EPSRC grant no. EP/K000586/1. The financial support by the LOCATE Project of *Hybrid Air Vehicles Ltd* and *Innovative UK* is gratefully acknowledged.

[1] Stockbridge, C., Ceruti, A., and Marzocca, P., "Airship Research and Development in the Areas of Design, Structures, Dynamics and Energy Systems," *International Journal of Aeronautical and Space Sciences*, Vol. 13, No. 2, 2012, pp. 170–187.

[2] Freeman, H., "Force Measurements on a 1/40-scale Model of the U.S. Airship 'AKRON'," *PhD Thesis, Cranfield Institute of Technology*, October 1990.

[3] Gomes, S., "An Investigation of the Flight Dynamics of Airships with Application to the YEZ-2A," *PhD Thesis, Cranfield Institute of Technology*, October 1990.

[4] Wang, X., Fu, G., D, P., and Shan, X., "Experimental Investigations on Aerodynamic Characteristics of the ZHIYUAN-1 Airship," *Journal of Aircraft*, Vol. 47, No. 4, July-August 2010.

[5] Suman, S., Lakshmipathy, S., and Pant, R., "Evaluation of Assumed-Transition-Point Criterion in Context of Reynolds-Averaged Simulations Around Lighter-Than-Air Vehicles," *Journal of Aircraft*, Vol. 50, No. 2, March-April 2013.

[6] Yamasaki, T. and Goto, N., "Identification of Blimp Dynamics via Flight Tests," *Transactions of the Japan Society for Aeronautical and Space Sciences*, Vol. 46, No. 153, 2003, pp. 195–295.

[7] Munk, N., "The Aerodynamic Forces on Airship Hulls," *NACA TR-184, Springfield, VA*, , No. 3, January 1924.

[8] Cook, M., Lipscombe, J., and Goineau, F., "Analysis of the Stability Modes of the non-rigid Airship," *The Aeronautical Journal*, Vol. 104, No. 1036, 2000, pp. 279–290.

[9] Carrion, M., Biava, M., Steijl, R., Barakos, G., and Stewart, D., "Analysis of Hybrid Air Vehicles Using Computational Fluid Dynamics," *Journal of Aircraft*, 2005.

[10] Woodgate, M. and Barakos, G., "Implicit Computational Fluid Dynamics Methods for Fast Analysis of Rotor Flows," *AIAA Journal*, Vol. 50, No. 6, 2012, pp. 1217–1244.

[11] Wang, X., "Computational Fluid Dynamics Predictions of Stability Derivatives for Airship," *Journal of Aircraft*, Vol. 49, No. 3, May-June 2012.

[12] Da Ronch, A., Vallespin, D., Ghoreyshi, M., and Badcock, K., "Evaluation of Dynamic Derivatives Using Computational Fluid Dynamics," *AIAA Journal*, Vol. 50, No. 2, February 2012.

[13] Mader, C. and Martins, J., "Computing Stability Derivatives and Their Gradients for Aerodynamic Shape Optimization," *AIAA Journal*, Vol. 52, No. 11, November 2014, pp. 2533–2545.

[14] Barakos, G., Steijl, R., Brocklehurst, A., and Badcock, K., "Development of CFD Capability for Full Helicopter Engineering Analysis," 31st European Rotorcraft Forum, Florence, Italy, 13-15 September 2005, .

[15] Woodgate, M. and Barakos, G., "Implicit CFD Methods for Fast Analysis of Rotor Flows," 36th European Rotorcraft Forum, Paris, France, September 2010, .

[16] Osher, S. and Chakravarthy, S., "Upwind Schemes and Boundary Conditions with Applications to Euler Equations in General Geometries," *Journal of Computational Physics*, Vol. 50, No. 3, June 1983, pp. 447–481.

[17] van Leer, B., "Towards the Ultimate Conservative Difference Scheme, V. A Second Order Sequel to Godunov's Method," *J. Comp. Phys.*, Vol. 32, 1979, pp. 101–136.

[18] Rieper, F., "A low-Mach number fix for Roe's approximate Riemann solver," *Journal of Computational Physics*, Vol. 230, March 2011, pp. 5263–5287.

[19] Carrión, M., Woodgate, M., Steijl, R., and Barakos, G., "Implementation of All-Mach Roe-type Schemes in Fully Implicit CFD Solvers - Demonstration for Wind Turbine Flows," *International Journal for Numerical Methods in Fluids*, Vol. 73, No. 8, 2013, pp. 693–728.

[20] Axelsson, O., *Iterative Solution Methods*, Cambridge University Press: Cambridge, MA, 1994.

[21] Menter, F. and Egorov, Y., "The Scale-Adaptive Simulation Method for Unsteady Turbulent Flow Predictions. Part 1: Theory and Model Description," *Flow Turbulence Combust*, Vol. 85, 2010, pp. 113âĂŞ138.

[22] Hellsten, A., "New Advanced k-ω Turbulence Model for High-Lift Aerodynamics," *AIAA Journal*, Vol. 43, No. 9, 2005, pp. 1857–1869.

[23] Zografakis, G. and Barakos, G., "Transition Modelling for Rotorcraft CFD," 34th European Rotorcraft Forum, Liverpool, UK, September 2008, .

[24] Klein, V., Murphy, P., Curry, T. J., and Brandon, J. M., "Analysis of Wind Tunnel Longitudinal Static and Oscillatory Data of the F-16XL Aircraft," Tech. Rep. NASA/TM-97-206276, National Aeronautics and Space Administration, Hampton, VA, USA, December 1997.

[25] Steijl, R. and Barakos, G., "Sliding Mesh Algorithm for CFD Analysis of Helicopter Rotor-Fuselage Aerodynamics," *Int. J. Numer. Meth. Fluids*, Vol. 58, October 2008, pp. 527–549.

[26] Menter, F., "Two-Equation Eddy-Viscosity Turbulence Models for Engineering Applications," *AIAA Journal*, Vol. 32, No. 8, 1994, pp. 1598–1605.